

# Preliminary design of a large angle beamstrahlung detector at CESR

N. Detgen, G. Bonvicini, D. Cinabro, D. Hartill,  
S. Henderson, G. Sun and J. Welch

*Laboratory of Nuclear Sciences, Cornell University, Ithaca NY 14853  
Wayne State University, Detroit MI 48201*

## Introduction

The beam-beam interaction at  $e^+e^-$  colliders is a subject that has generated hundreds of papers over the years. As the beams become smaller at new machines, and luminosity becomes the dominant parameter to assess the scientific value of a machine, new effects become apparent in the beam-beam interaction that affect the luminosity output.

An important subset of these effects are those situations where beams collide asymmetrically. As Fig. 1 shows, there are seven geometric degrees of freedom (*dof*) in such an asymmetric collision. One more *dof* is to be added if one considers not only the beams relative rotation, but also the rotation with respect to the machine transverse axes. It is these *dof* that a large angle beamstrahlung detector would map. Effects that depend primarily on the beam current are not studied here, as beam current is effectively monitored by other means.

Of the degrees of freedom in Fig. 1, four or five are of interest at CESR. Such a large dimensionality is best studied with a beam-beam monitor that observes at once several observables which are related to the geometrical *dof*. A large angle beamstrahlung detector measures just that. Since all future  $e^+e^-$  machines are completely asymmetric, this technique might have long-range implications for the field.

In Section 2 the theory of beamstrahlung is reviewed, focussing on the aspects that affect observability and pattern recognition. Beam-beam monitoring which assume symmetric beams is also reviewed. In Section 3 the monitoring of asymmetric beams is reviewed. In Section 4 the backgrounds and their modeling is discussed. In Section 5 a possible detector design is introduced. Conclusions are in Section 6. People interested in issues affecting the feasibility of the detector should simply read Section 4 and Appendix B.

## 1 General properties of beamstrahlung.

The power emitted in a collision by two perfectly overlapping, Gaussian beams was first derived in Ref.[1] and reads

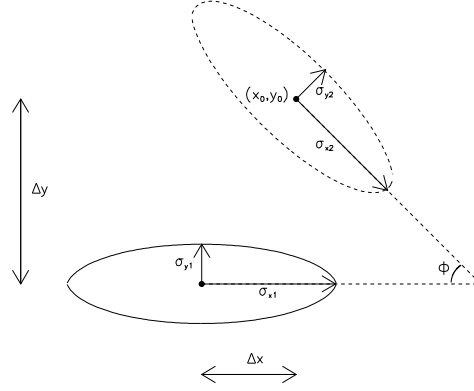


Figure 1: A general beam-beam collision. Seven parameters can be seen, corresponding to two transverse dimensions for each beam, a two dimensional impact parameter vector connecting the two beam centers, and one relative rotation in the transverse plane.

$$W_1 = fU_1 \quad (1)$$

$$= g(r)r_e^3 mc^2 \gamma^2 \frac{fN_1 N_2^2}{4\pi \sigma_x \sigma_y \sigma_z} \quad (2)$$

$$= g(r)r_e^3 mc^2 \gamma^2 \frac{LN_2}{\sigma_z}, \quad (3)$$

where  $U_1$  is the energy radiated per collision. The origin of the powers of the beam charges in the Equation above is discussed in Appendix A. Here  $r_e$  is the classical radius of the beam particles,  $m$  their mass, and  $\gamma = E/m$  the relativistic factor.  $g(r)$  is a dimensionless factor obtained in the integration over space-time, equal to[1]

$$g(r) = \frac{64\sqrt{\pi}r}{3\sqrt{3r^4 - 10r^2 + 3}} \arctan\left(\frac{\sqrt{3r^4 - 10r^2 + 3}}{3r^2 + 8r + 3}\right).$$

It is maximal for round beams ( $r = 1$ ), at 2.735, and for flat beams ( $r$  small) it can be approximated as follows

$$g(r) \sim 11.4r.$$

In the case of flat beams (as in CESR),  $\sigma_y$  cancels in Eq. 2 and the dependence of  $W$  on beam parameters becomes

$$W \propto \frac{\gamma^2 N_1 N_2^2}{\sigma_z \sigma_x^2}. \quad (4)$$

At CESR Phase III, 7W of beamstrahlung power is produced, which is dwarfed by the various sources of synchrotron background near the IR.

At the SLC, a beamstrahlung signal was obtained[2] by exploiting the difference between the beam magnetic field (10-100  $T$ ) and the other magnetic fields along the beam line (0.1- 1  $T$ ). The larger magnetic fields resulted in a higher cutoff energy for beamstrahlung, and a favorable signal/noise could be obtained for photons of approximately 20 MeV energy. At CESR, the magnetic field of the beams and of the magnets along the beam line have the same order of magnitude (0.1  $T$ ), eliminating this possibility. The wider angular spread of beamstrahlung radiation, compared to normal synchrotron radiation, is used instead.

A first application of a beamstrahlung detector sensitive only to the total power (Eq.4), would be the instantaneous measurement of  $\sigma_x$ , assuming a constant  $\sigma_z$ , or the measurement of  $\sigma_z$  during machine development, if the beam optics are kept fixed.

Dependence on the third beam parameter  $\sigma_y$  is nearly lost in the total power, if the beams are flat, but  $\sigma_y$  can be measured very precisely with a simple scan of one beam across the other. The power of both beams changes according to Fig. 2, producing a camelback plot that has been widely used in the study of beamstrahlung[2]. For small aspect ratios  $r$ , the peak-to-valley distance  $d$  in Fig. 2 and  $\sigma_y$  are related[3]

$$d \sim 3.97\sigma_y(1 - 5.4\epsilon). \quad (5)$$

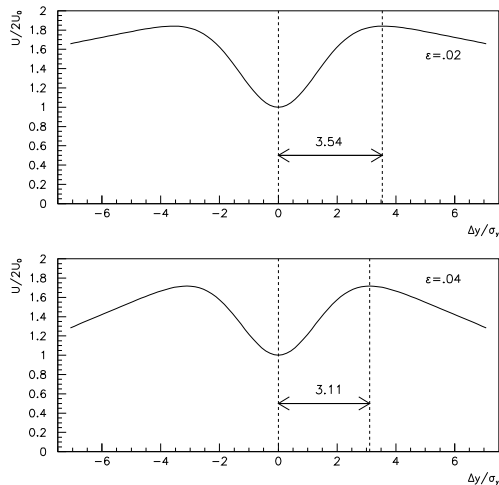


Figure 2: Normalized power emitted in beamstrahlung, as a function of normalized  $y$ -offset. a)  $\epsilon = 0.02$ . b)  $\epsilon = 0.04$ . The distance from minimum to maximum is shown, in units of  $\sigma_y$ .

Currently, the CESR beams are artificially perturbed with an amplitude of order  $0.01\sigma_y$  to measure the beam-beam interaction by observing the effect of the perturbation on the other beam via the lock-in effect[4]. It is conceivable that this technique could ultimately be used to determine  $\sigma_y$  without scanning. Note that a beam scan could also be used to measure  $\sigma_x$  separating it from  $\sigma_z$ .

The large-angle power emitted as a function of angle and frequency is expressed as [1]

$$I(\theta, \phi, \omega) = \frac{3\sigma_z W_1}{4\pi\sqrt{\pi}c} \frac{1}{\gamma^4\theta^3} \exp\left(\frac{-\sigma_z^2\theta^4\omega^2}{16c^2}\right). \quad (6)$$

The large angle power is proportional to the total power, times known or constant integration factors. At a fixed angular location, the spectrum is strongly dependent on  $\sigma_z$ , providing a purely shape-like method to determine the beam length.

The exponential factor in Eq.6 is of fundamental importance for this project. An exponential dependence on the magnet length is always present at large angle[5]. CESR magnets are typically one hundred times longer than the beams, resulting in a much more collimated synchrotron beam, and a favorable signal/noise ratio can be obtained at a large enough angle. As an added bonus, the large angle beamstrahlung power scales like  $1/\gamma^2$ , so that the large angle method, which had a marginal signal at the SLC[6], yields a much stronger signal at a lower energy collider.

## 2 Information content of large angle polarization.

At large angle, the dependence of the polarization on azimuth reads as [3]

$$I_{\perp}(\theta, \phi, \omega) = I(\theta, \phi, \omega) \frac{U_{\perp} \cos^2(2\phi) + U_{\parallel} \sin^2(2\phi)}{U}, \quad (7)$$

$$I_{\parallel}(\theta, \phi, \omega) = I(\theta, \phi, \omega) \frac{U_{\perp} \sin^2(2\phi) + U_{\parallel} \cos^2(2\phi)}{U}. \quad (8)$$

The  $U$  form factors are defined as

$$U_{\perp} + U_{\parallel} = U(r, \vec{v}), \quad U(r, \vec{0}) = g(r)/2.$$

The vector  $\vec{v}$  represent the various *dof* depicted in Fig. 1, and  $\vec{v} = 0$  represents the perfect collision conditions. The azimuthal angle, and the perpendicular and parallel components of power, are calculated with respect to the direction of the bending force. The azimuthal dependence of the polarization is purely a kinematic effect[3].

In the Equation above, if both beams are allowed to rotate away from the nominal axes, the azimuthal angle should be replaced by  $\phi - \phi_0$ . Thus at least three components, one of which should be measured at a different angle from the other two, are needed to solve for the system.

If a detector is to be built, it will not generally measure the components perpendicular and parallel to the bending force, but rather the components along some axes, which are most naturally chosen to be the  $x$ - and  $y$ - axis of CESR. Further, one assumes that beamstrahlung yields can be normalized against expectation values, based on machine history, so that one measures the normalized form factors  $U_x$  and  $U_y$  which can be combined into vectors  $\mathbf{U}_1$  and  $\mathbf{U}_2$ , one for each beam.

The  $\mathbf{U}_1, \mathbf{U}_2$  vectors are used to construct the so-called beamstrahlung diagram, which consists of the two vectors being plotted together. If the beams are overlapping perfectly, the radiation as a whole is unpolarized[1], and the two vectors overlap perfectly at (1,1) (Fig. 3). In practice, beams change dynamically during the collision and slightly more power is radiated in  $y$  than in  $x$ , changing the perfect collision angle from 45 to 45.5 degrees[3].

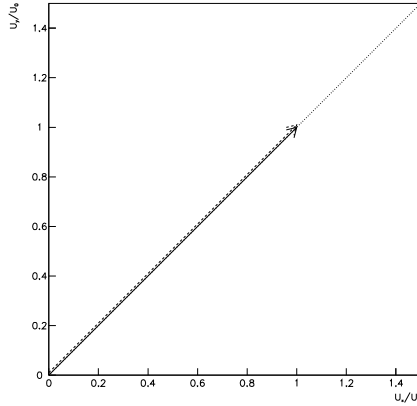


Figure 3: The beamstrahlung diagram corresponding to a perfect beam-beam collision. The two vectors are exactly equal. The dashed arrow is slightly displaced for display purposes.

Fig. 4 and 5 show the effect of asymmetric beam-beam collisions on the diagram. There is a clear one-on-one relation between a pattern and a type of asymmetry (which have been ordered by dominant multipole components). As discussed in Ref.[3], positively-defined dimensionless asymmetries are defined from the diagrams, their value is measured, and a beam correction can be computed.

Fig. 6 and 7 show what happens when multiple pathologies are observed. The diagrams are now no longer unique, but the result of a detailed calculation[3] shows that, as long as the pathologies are corrected in hierarchical order, the diagram will evolve in a unique way. Because of the different evolution after the first correction, Ref.[3] claims that the four-dimensional diagram effectively monitors a six-dimensional parameter space.

### 3 Background calculations.

We choose for our detector a location between 5 and 6 meters from the IP. With the help of Yulin Li we identified open locations at 5.3 and 5.6 meters. The 5.6 meters location was subsequently chosen. Here the beam pipe is round and has an inner radius of 6.36cm. Assuming a square primary mirror with the outer edge at the beam pipe, with a solid angle acceptance of  $(1\text{mrad})^2$ , the inner edge is located at 5.80 cm, 1.70 cm outside the stay clear envelope.

In the following we assume that our optical system, and in particular the primary mirrors, are of laser-optics quality, and that only the backgrounds entering the detector within the optical acceptance will contribute. This corresponds to an effective solid angle efficiency of about  $10^{-7}$  for isotropic radiation. The mirrors image strips of beam pipe on the other side of the interaction region, opposite in azimuth, centered around 5.6 meters, 60 centimeters long and 1.12 centimeters wide. These strips are called in the following the “field-of-view” (FOV). One is particularly concerned about radiation striking the mirrors or the FOV.

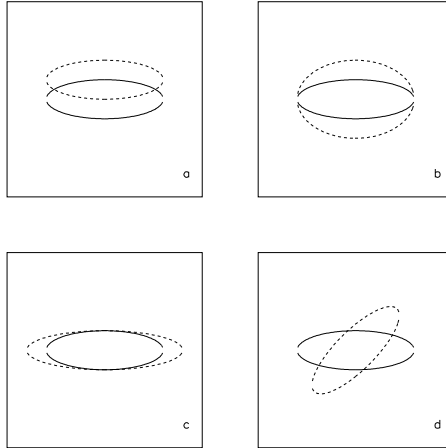


Figure 4: The four beam-beam pathologies that lead to wasted luminosity; a) a  $y$ -offset; b)  $y$ -bloating; c)  $x$ -bloating; and d) a beam-beam rotation. The pathological beam is represented by the dashed ellipse.

Radiation backgrounds at the chosen location are small. The synchrotron sweep from the incoming beam deposits about one Watt per centimeter. About  $10^{-5}$  of the total radiation is in the infrared frequency window chosen. The mirrors inner edges are located at 4.2 and 5.0 centimeters above the horizontal plane, and are not hit directly by the sweep. The outgoing sweep does not contribute significantly, and its backscattered radiation can be discriminated by timing.

The dominant source of synchrotron radiation striking the primary mirrors are the superconducting quadrupoles, whose radiation was the object of a careful simulation. The beam line and beam optics used were the nominal Phase III conditions. Beam position was varied in  $x$  between -2.2 and 0 mm, and the beam crab angle was simulated between 1.5 and 3 mrad. A 1 mrad bump in the vertical trajectory was also simulated.

Backgrounds were computed at various detection locations, located at 30, 60, 90, 120 and 150 degrees with respect to the  $x$ -axis. The 30 degree location is the outermost one, and the 150 degrees the innermost one with respect to the CESR ring. The typical total power striking the mirrors varies from 0.1pW at 60 degrees to  $10\mu\text{W}$  at 150 degrees.

After identifying the 60 degrees region as the optimal one, simulations were run with counters placed between 40 and 80 degrees, one every ten degrees. The final choice of azimuth for the two detectors were 50 and 72.5 degrees.

The detectors were placed at an appropriate location in  $z$  and transverse radius  $r$ , and were assumed to be square holes with 1mrad opening in  $\theta$ . The beam was simulated out to  $10\sigma$  in both  $x$  and  $y$ , and was transported across the quadrupoles. At each step, the angle between electron and detector, and the bending force were computed. Using prepared lookup tables, the power to each detector location, within a specified frequency window, was calculated and

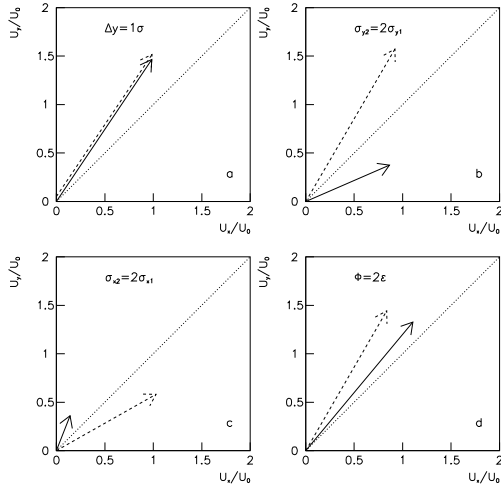


Figure 5: Beamstrahlung diagrams corresponding to the four pathologies of Figure 4. The tips of vectors in part a are displaced for display purposes. Stiff beams are assumed.

summed. Later, only the fraction of power entering the detector within the angular acceptance was considered for final background results.

Because the beams enter and exit the IP at an angle in the  $x - z$  plane, pointing inward with respect to CESR, for each simulation the 150 degrees counter had the smallest effective angle with respect to the beam direction, and the 30 degrees counter the largest.

The synchrotron backgrounds were computed according to the methods described in Ref.[5]. Briefly, the radiation could be distributed according to Jackson’s “searchlight” approximation[7], or according to Coisson’s “short magnet” approximation[8]. These approximations are extreme: the former assumes that the electron is sweeping in its bending plane, effectively covering all angles above a minimum, the second assumes that the angle between detector and electron remains fixed. We found that the two approximations yielded the same results (to within 20%) for the quadrupoles in the visible region. The short magnet approximation yielded always the largest backgrounds, particularly in the infrared region, and was used to produce the plots shown below.

The first issue we addressed was the geometrical source of the backgrounds. Generally, we expect no backgrounds from the center of the quads, where there is no field, and the extreme tails, where there is no charge. There must be a maximum in between. Fig. 8 shows that generally backgrounds came from well-defined regions within the quadrupoles, where the particle’s angle with respect to the axis is maximal, and two to five standard deviations away from the center. For both the incoming and outgoing beam, the particles producing the most background are those pointing in the general direction of the counter. Because of that, the background is strongly polarized. The power with tangential polarization is typically one order of magnitude lower than the power polarized radially.

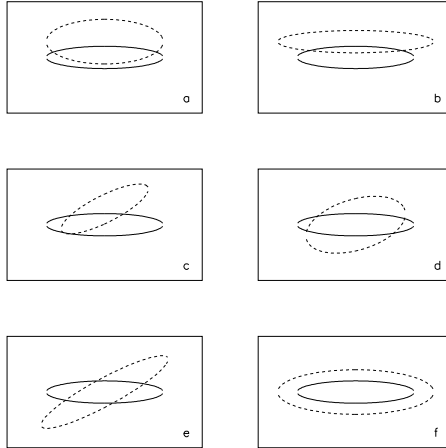


Figure 6: The six possible configurations arising from combinations of any two of the pathologies of Figure 3. a)  $y$ -offset and  $y$ -bloating. b)  $y$ -offset and  $x$ -bloating. c)  $y$ -offset and beam-beam rotation. d)  $y$ -bloating and beam-beam rotation. e)  $x$ -bloating and beam-beam rotation. f)  $y$ -bloating and  $x$ -bloating.

We also observed clear sunshine/shade effects for the incoming beam. These were traced mostly to the masks placed near the IP. Unfortunately, no such effect exists for the outgoing beam, which dominates the background for counters at 120 and 150 degrees.

When studying the signal/noise ratio, we tried to implement the “magic angle” strategy of Ref.[9]. Basically, given the wavelength at which one wants to observe beamstrahlung (“red”), the detector is placed at the angle at which the exponent in Eq.6 is equal to -2. At half the wavelength (“blue”), the exponent will be equal to -8 and a measure of the “blue” will measure backgrounds, while the “red” measures both signal and background. In theory, it was hoped that we could work with real red ( $\lambda = 660\text{nm}$ ) and blue ( $\lambda = 330\text{nm}$ ) light, so that standard photomultipliers could be used.

In practice, we found that the beamstrahlung yield in the red exceeds the synchrotron radiation background only when the signal becomes very weak ( $10^{-14}\text{W}$ , or  $10^{-2}$  photons per beam crossing). Fig. 9 shows the signal and background (separately for incoming and outgoing beam) for  $570 < \lambda < 630\text{nm}$ . The gaussian dropoff of the signal is very obvious. Following Ref.[9], we moved to higher wavelengths and angles (both need to increase to keep the exponential factor in Eq.6 approximately constant). We still use red light as the background control sample.

Next we tried the near infrared,  $1.2 < \lambda < 1.4\mu\text{m}$ . Table 1 shows the infrared power striking the mirrors, and the power within the angular acceptance of the telescope, for each of the five counters, and for various beam parameters and also different optics. Nominal conditions were assumed to be:  $x_{IP} = -2\text{mm}$ ,  $x'_{IP} = -2.2\text{mrad}$ ,  $\sigma_z = 18\text{mm}$ , and  $I_{beam} = 0.5\text{A}$ .  $y_{IP}$  and  $y'_{IP}$  were kept equal to zero except for a series of simulation were a positive and negative  $1\text{mrad}$   $y$ -bump was simulated (see Table 1). A different lattice was also tried for the purpose



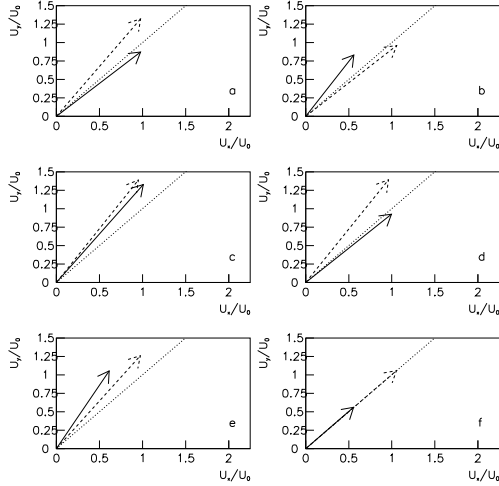


Figure 7: Beamstrahlung diagrams corresponding to Figure 6.

of assessing the impact of changing the optics on the background. Other beam parameters (relevant for the beamstrahlung signal) are  $\sigma_x = 10\mu\text{m}$ ,  $\sigma_y = 450\mu\text{m}$ , and  $f = 17\text{MHz}$ .

Three features emerge from Table 1:

- for all simulations, there is a strong dependence of the power on the azimuth.
- for all simulations, there is a low background region in the vicinity of the 60 degrees counter.
- for all simulations, the background is strongly polarized ( $\approx 90\%$ )

Figs. 10 and 11 show signal and background for  $1.2 < \lambda < 1.4\mu\text{m}$ , for counters placed at 50 and 72.5 degrees respectively. There are three reasons to be satisfied with this plot:

- the signal does not change much when beam conditions change around  $\theta = 11\text{mrad}$ . In turn, this limits the dynamic range requirements for our counters.
- the signal exceeds the background well to the left and to the right of  $\theta = 11\text{mrad}$ , making the signal/noise nearly independent of beam conditions. At the nominal CESR conditions one gets a flux of  $5 \times 10^7$  photons per counter per second, or 3 per collision.
- At 5.6 meters, the beam pipe is seen at an effective angle of about 11 mrad, which is close to the angle of choice. One can minimize the mirror protrusion inside the pipe.

The detector must be sensitive to the near infrared. On the other hand, the advantages of the chosen working point, in particular the minimal impact on the beam pipe, make this the best choice for CESR.

Collision conditions (mm,mrad)	Counter Azimuth	$W_{rad.}(W)$	$W_{tan.}(W)$
Nominal(see text)	30	$2 \times 10^{-32}$	$1 \times 10^{-33}$
Nominal	60	$4 \times 10^{-24}$	$3 \times 10^{-25}$
Nominal	90	$1 \times 10^{-9}$	$9 \times 10^{-11}$
Nominal	120	$2 \times 10^{-11}$	$2 \times 10^{-12}$
Nominal	150	$4 \times 10^{-26}$	$5 \times 10^{-27}$
$x_{IP} = -2.2, x'_{IP} = -3$	30	$9 \times 10^{-25}$	$5 \times 10^{-26}$
$x_{IP} = -2.2, x'_{IP} = -3$	60	$1 \times 10^{-17}$	$1 \times 10^{-18}$
$x_{IP} = -2.2, x'_{IP} = -3$	90	$1 \times 10^{-11}$	$1 \times 10^{-12}$
$x_{IP} = -2.2, x'_{IP} = -3$	120	$2 \times 10^{-8}$	$2 \times 10^{-9}$
$x_{IP} = -2.2, x'_{IP} = -3$	150	$2 \times 10^{-8}$	$2 \times 10^{-9}$
$x_{IP} = 0, x'_{IP} = -1.5$	30	$9 \times 10^{-21}$	$6 \times 10^{-22}$
$x_{IP} = 0, x'_{IP} = -1.5$	60	$4 \times 10^{-14}$	$3 \times 10^{-15}$
$x_{IP} = 0, x'_{IP} = -1.5$	90	$2 \times 10^{-9}$	$2 \times 10^{-10}$
$x_{IP} = 0, x'_{IP} = -1.5$	120	$6 \times 10^{-8}$	$7 \times 10^{-9}$
$x_{IP} = 0, x'_{IP} = -1.5$	150	$3 \times 10^{-9}$	$3 \times 10^{-10}$
$y'_{IP} = -1$	30	$2 \times 10^{-31}$	$8 \times 10^{-33}$
$y'_{IP} = -1$	60	$5 \times 10^{-25}$	$3 \times 10^{-26}$
$y'_{IP} = -1$	90	$6 \times 10^{-10}$	$5 \times 10^{-11}$
$y'_{IP} = -1$	120	$1 \times 10^{-12}$	$9 \times 10^{-13}$
$y'_{IP} = -1$	150	$4 \times 10^{-26}$	$4 \times 10^{-27}$
$y'_{IP} = +1$	30	$2 \times 10^{-33}$	$3 \times 10^{-34}$
$y'_{IP} = +1$	60	$4 \times 10^{-23}$	$2 \times 10^{-24}$
$y'_{IP} = +1$	90	$2 \times 10^{-9}$	$1 \times 10^{-10}$
$y'_{IP} = +1$	120	$3 \times 10^{-11}$	$3 \times 10^{-12}$
$y'_{IP} = +1$	150	$4 \times 10^{-26}$	$4 \times 10^{-27}$
New lattice	30	$7 \times 10^{-32}$	$5 \times 10^{-33}$
New lattice	60	$1 \times 10^{-29}$	$3 \times 10^{-30}$
New lattice	90	$4 \times 10^{-11}$	$4 \times 10^{-12}$
New lattice	120	$5 \times 10^{-13}$	$4 \times 10^{-14}$
New lattice	150	$6 \times 10^{-27}$	$6 \times 10^{-28}$

Table 1: Power absorbed by the primary mirrors at various azimuthal locations. Nominal beam conditions are discussed in the text. Changes in beam optics are listed in the first column. The two power columns are the radial and tangential polarization components for the power within the acceptance of the optical system.

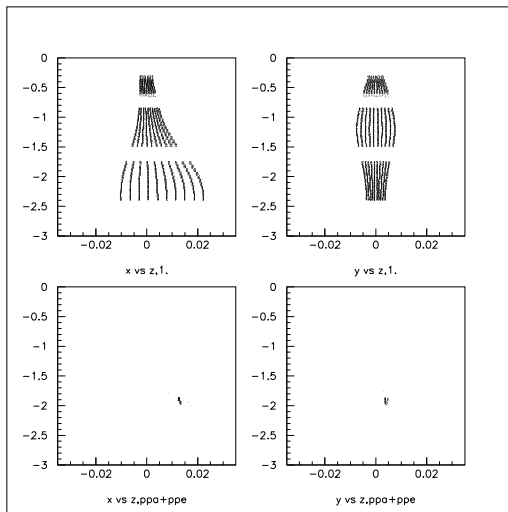


Figure 8: Incoming beam trajectory through the IR quadrupoles. The top two plots show respectively the  $x - z$  and  $y - z$  projections. The lower two plots show where the radiation hitting the 120 degrees counter is coming from. For this simulation, the 120 degrees counter was placed at 6 mrad from the beam line.

The conclusion that the signal dominates over the background in the phase space region chosen is supported by the following considerations:

- the background estimate does not depend appreciably on the synchrotron radiation model used. The two models are extreme in their assumptions about the angular dependence of the Fourier transform, effectively placing limits on the true value of the background.
- the background comes predominantly from particles that point to the vicinity of the counter. The two models tend to be in rough agreement at low and medium angle.
- the background comes principally from the medium beam tails ( $2-5\sigma$ ). These are unlikely to be poorly simulated.
- the background is still much smaller than the signal when the beams angles and positions are changed.
- the background is still much smaller than the signal when the lattice is changed.

Finally, we wish to estimate smaller sources of background. Cherenkov radiation from the vacuum window is almost certainly negligible. The detector is located in a place where stray electrons strike seldom. The CESR beam loses typically one particle for every ten meters of flight, most of them at collimators located away from the region under consideration. The very small solid angle between window and counters further discriminates against Cherenkov radiation, which peaks at lower wavelengths and forward angles. Even if our detector is occasionally

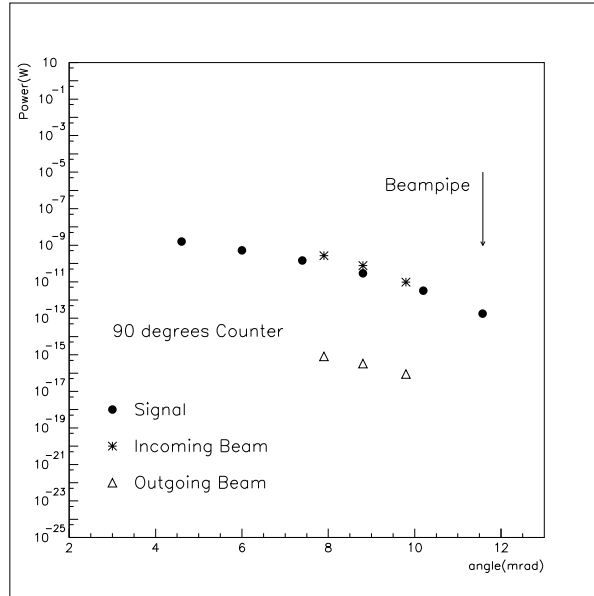


Figure 9: Power versus angle in the red wavelength, for the 90 degrees counter. Black dots: beamstrahlung power. Stars: incoming beam. White triangles: outgoing beam.

sprayed, a readout system that eliminates very large pulses will make sure that this source of background is eliminated.

Black body radiation is also negligible, as long as the photomultipliers are cooled to  $-80^{\circ}\text{C}$ , as described in the next Section. All other sources of thermal photons do not have enough solid angle to contribute.

Isotropic radiation, in the form of fluorescence and Thomson scattering, is discussed in Appendix B, and found to be very negligible.

Thus one is left to consider synchrotron radiation which is rescattered at low angle by the beam pipe, and somehow aligns itself with the telescope's angular acceptance. The last scattering must happen in the FOV.

The beam pipe near the FOV is shaped as in Fig. 12. It maintains a constant  $x$ -axis, but the  $y$ -axis decreases from 12.72 centimeters down to 8.00 centimeters. The wide section is towards the IP, and the narrow section away from the IP. The funnel section is located between 6 and 6.22 meters from the IP. The FOV is located to the right of the funnel, at 5.6 meters. The drawing illustrates how our FOV is shaded from incoming radiation by the beam pipe funnel.

The FOV can be illuminated directly only by radiation originating in the last meter in the narrow section, with a corresponding radiating angle of at least 40 mrad. Clearly the FOV will be illuminated directly in a negligible way.

More relevant is the radiation, generated upstream, that scatters against the beam pipe in the last meter before the funnel, then scatters in the FOV while aligning itself with the telescope's acceptance. For the first scattering, the incident angle is of order 1 mrad and the

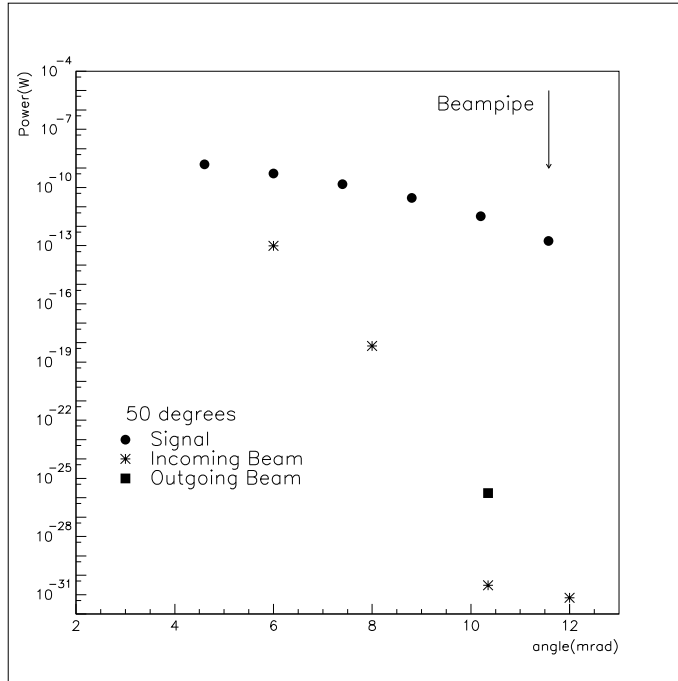


Figure 10: Power versus angle in the infrared region, for a mirror located at 50 degrees. Black dots: beamstrahlung power. Stars: incoming beam. White triangles: outgoing beam.

reflecting angle about 40 mrad. For the second scattering, the incident angle is about 40 mrad, and the reflecting angle is 11 mrad. Between the two scattering, the infrared photon direction must be rotated in  $\phi$  by about 60 degrees.

This effect is clearly small, but cannot be computed reliably. In principle, if the FOV were a perfect mirror, this source of background would be zero. In practice, one can measure this effect with a bench test. A factor of about  $10^{-9}$  reduction is needed from the two rescatterings to make this source of background smaller than the signal. It is possible that the choice of infrared wavelengths will help us, because the beam pipe will be a better mirror at longer wavelengths. We propose to measure light scattering off the pipe at WSU over the Fall to assess this source of background. Alternatively, one could consider electropolishing the inside of the beam pipe at that location, for the purpose of improving its reflectivity and minimize rescattering. According to Yulin Li, modifying the inside structure of the beam pipe (with a stack of short razor blades to stop rescattered light) would be difficult mechanically.

## 4 Detector design.

The beamstrahlung optics starts with two mirrors located in the lower half of the beam pipe, at -50 and -72.5 degrees with respect to the  $x$ -axis, 5.6 meters away from the IP (Fig. 13).

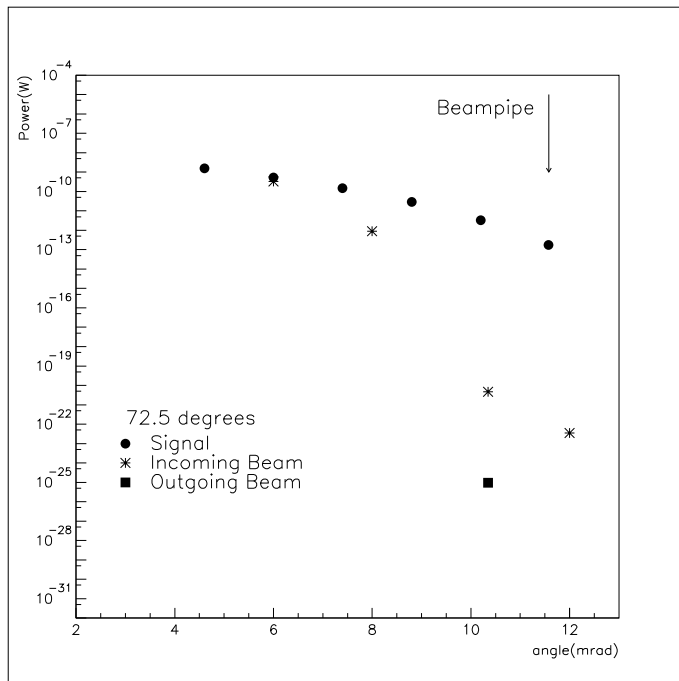


Figure 11: Power versus angle in the infrared region, for a mirror located at 72.5 degrees. Black dots: beamstrahlung power. Stars: incoming beam. White triangles: outgoing beam.

The mirrors are square, with sides of 5.6 millimeters, and they reflect light straight up through vacuum windows of diameter 8 millimeters. Virtually all material candidates for the window are fully transparent in the 1.2-1.4 $\mu\text{m}$  region.

Light travels up for 60 centimeters, before being collimated to obtain only the component between 10.4 and 11.4 mrad, and then is reflected back to its original direction to recover full polarization information.

A calcite cube splitter can efficiently separate the two polarization components over a wide spectrum. Each polarized beam is then split into two with partially reflecting mirrors. Of the four beams, two are now used for infrared detection, and two for red light. The former is separated using laser mirrors which reflect only between 1.2 and 1.4 microns for the last reflection. The latter needs no filtering as the photomultiplier photocathode provides a natural cutoff at 0.7 microns. There are four PMTs per viewport, and sixteen total in the system.

Infrared sensitive PMT have been made available by Hamamatsu, with a non-zero quantum efficiency extending to 1.7 microns. They must be operated at  $-80^{\circ}\text{C}$  for best noise performance. The cathode has a typical quantum efficiency of 1.0% in the infrared and 2.0% in the red, the typical gain is  $10^6$ , and the typical dark count is 20KHz. The dynodes are line focused, with a total pulse width of 5 nanoseconds. A factor of ten reduction in dark noise could be obtained by fast-gating the signal.

With the viewports and frequency windows described above, one obtains a signal of  $3 \times 10^5$

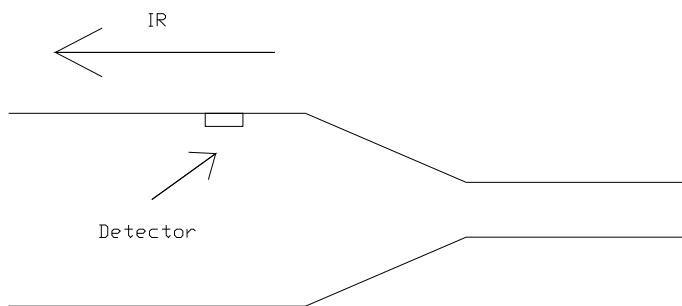


Figure 12: Beam pipe profile near the beamstrahlung detector location. The IP is located to the left of the funnel. The beamstrahlung detector is located to the left of the funnel, at 5.6 meters from the IP. The funnel itself is located between 6.00 and 6.22 meters from the IP.

photoelectrons per second for the phototubes looking at infrared light, and a much smaller one for the phototubes looking at red light. The total current for each infrared phototube is 100 nA. A 1% measurement of a single bunch will take approximately 1.5 seconds.

There seems no need for a Fast ADC, since most beam crossings will give zero photoelectrons. A gated discriminator, coupled to a microprocessor for fast hit counting, should suffice.

The total cost for such a monitor is estimated to be 10K, assuming that Dewars could be found for photomultiplier cooling.

## 5 Conclusions.

In conclusion, a large angle beamstrahlung detector for CESR appears feasible, and would provide important real time information on the beam-beam collision conditions. It is quite possible that the information could in turn produce improvements at the 10% level in the luminosity delivered by CESR, and it would improve our knowledge of beam-beam physics. Given the minimal cost and beam pipe disruption, we strongly recommend that it be built and implemented.

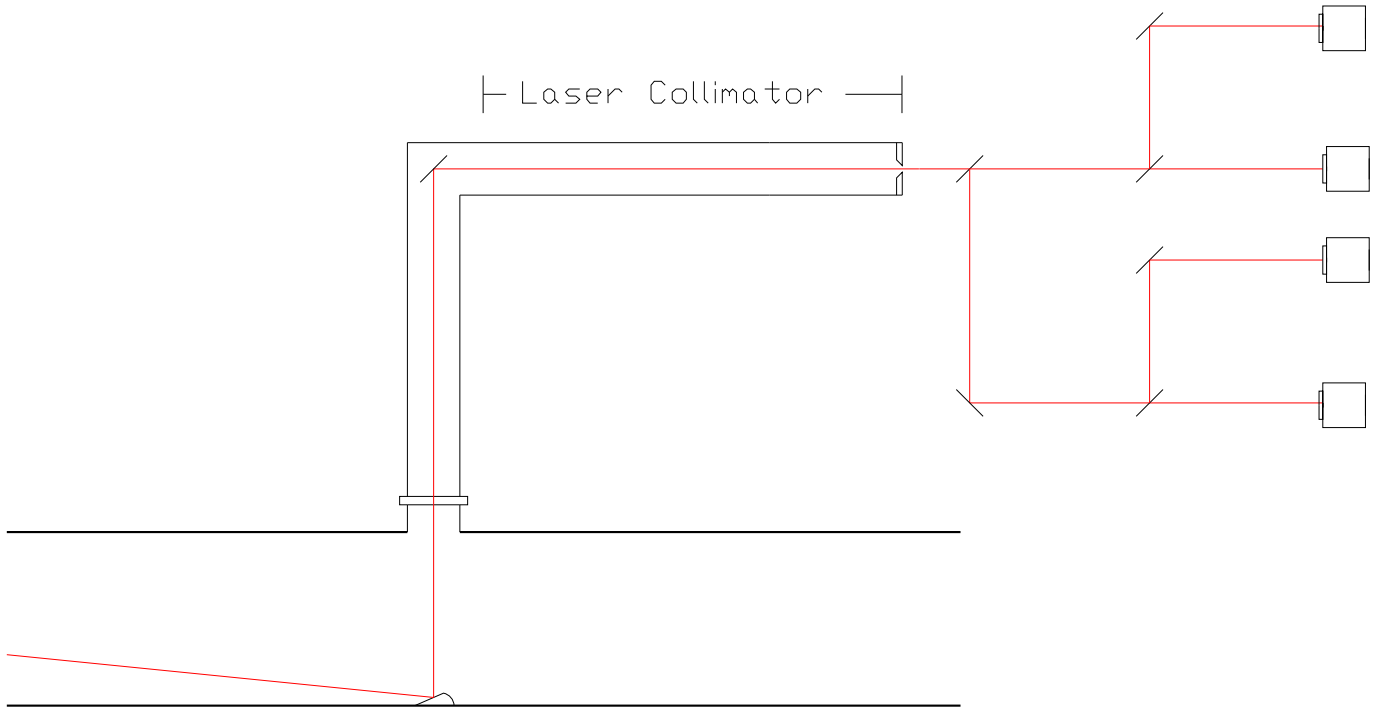


Figure 13: Preliminary design of the beamstrahlung detector. Shown are the primary mirror, vacuum window, two collimators, and four optical channels corresponding to the two polarizations and two frequency windows described in the text.

## Appendix A.

A group of particles being deflected in a magnet may radiate coherently. The purpose of this Appendix is to show that the radiation will always be linear with the radiating charge, if the wavelength under consideration is much smaller than the beam length.

Let us consider a CESR beam ( $\sigma_z = 18\text{mm}$ ), undergoing a 20 mrad deflection in a 1 meter long dipole, and let us consider radiation in the near infrared ( $\lambda = 1\mu\text{m}$ ), detected at  $\theta = 10\text{mrad}$  at a distance  $D = 6$  meters. The coherence length  $d$  is the path, along the beam trajectory, for which photons from the same electron will arrive in phase at the detector (for the purpose of this discussion, within a tenth of a wavelength). A simple geometrical calculation gives

$$d \sim \left(\frac{\lambda}{10}\right) \frac{2}{\theta^2} = 2\text{mm},$$

so that a substantial fraction of the beam is radiating coherently.

If that is the case, two electrons which are aligned in the transverse space but are separated longitudinally by half a wavelength will interfere destructively even in the dipole case, whereas those separated by one wavelength will interfere constructively.

Because the beam charge is very large, there would seem to be completely destructive interference, as the sum of the waves from each particle tends to zero. However interfering cells



will not possess the same charge due to statistical fluctuations, so that the effective radiating charge is  $\propto \sqrt{N}$ . This charge will then radiate coherently, yielding a total intensity

$$I(\theta, \phi, \omega) \propto (\sqrt{N})^2,$$

or a linear dependence on the radiating charge. Thus one is justified in treating a beam, much longer than the observed wavelength, as an ensemble of incoherent particles.

If we were to consider wavelengths longer than the beam length, we would indeed obtain

$$I(\theta, \phi, \omega) \propto N^2,$$

as the beam does behave like an antenna.

In the case of quadrupole (and also beamstrahlung) radiation, a particle located at  $(x, y, z)$  will interfere destructively with a particle located at  $(x, y, z + \lambda/2)$  and a particle located at  $(-x, -y, z)$ , which is undergoing an equal and opposite bending. Just the same the typical difference in population between interfering cells will be  $\propto \sqrt{N}$ , yielding the same result as above. Our beamstrahlung formulae have been derived for incoherent particles.

In conclusion, coherence effects, amongst them quadrupole radiation, become important at CESR only when wavelengths longer than the beam length are observed. A similar derivation of the power dependence on beam charge can be found in Ref.[10].

## Appendix B.

In this Appendix two sources of large angle rescattered radiation are discussed, as they have been mentioned as possible sources of backgrounds. Both of these sources of backgrounds suffer large solid angle inefficiencies, if the optical system really has an acceptance of  $(1\text{mrad})^2$ , or  $10^{-7}$  of the solid angle. Also in both cases radiation that is rescattered beyond the beam pipe skin depth will be reabsorbed by the metal before it can emerge. The skin depth of aluminum in the near infrared is about 1 nanometer.

Thomson scattering can rescatter photons elastically, off of surface electrons in the beam pipe. There is a weak angular dependence  $(1 + \cos^2 \theta)$  in Thomson scattering which can be ignored for our purposes. The total cross section is

$$\sigma = \frac{8\pi}{3} r_e^2 \sim 0.67 \text{ barns},$$

corresponding to a mean free path of 2 millimeters in aluminum. The total infrared power impinging on the mirrors can be obtained from the simulations presented in Table 1. We assume here  $10^{-5}$  pW, yielding a total background power of

$$W_T = W_{\text{mirror}} \epsilon_{\text{depth}} \epsilon_{\Omega} \sim 10^{-30} W,$$

which is very negligible. One watt of rescattered infrared radiation should hit the mirrors or any other part in the optical field for this effect to become an issue. Clearly this is a negligible source of backgrounds.

Beam pipe fluorescence can be studied using the information gathered for the beamstrahlung detector at the SLC[11]. As mentioned in the text, the 60 degrees mirror is struck by approximately 1pW in total power. At CESR, the typical attenuation length for synchrotron radiation

in the beam pipe is 1 micron. A typical conversion factor for the energy deposited in the metal, which is turned into fluorescence, is  $10^{-3}$ . Of the fluorescent energy, only no levels are present in aluminum within the specified frequency window[12], though we assume a fraction of  $10^{-3}$ . Putting all the factors together one obtains for the mirror fluorescence

$$W_F = W_{mirror} \epsilon_{depth} \epsilon_{\Omega} \epsilon_E \epsilon_{IR} \sim 10^{-25} W.$$

This result suggests that an infrared photomultiplier, placed in the South Ring and observing the inside of the beam pipe at large angle, should observe no counts, if all possible sources of stray reflection into the viewport can be eliminated.

## References

- [1] M. Bassetti *et al.*, IEEE Trans. Nucl. Science 30: 2182, 1983.
- [2] G. Bonvicini *et al.*, Phys. Rev. Lett. 62: 2381, 1989.
- [3] G. Bonvicini, D. Cinabro and E. Luckwald, Phys. Rev. E 59: 4584, 1999.
- [4] D. Sagan, J. Sikora and S. Henderson, CBN-97-13.
- [5] G. Bonvicini, CBN-98-12.
- [6] G. Bonvicini *et al.*, SLAC-PUB-3978.
- [7] J. D. Jackson, "Classical Electrodynamics", Wiley, Chapter 14.
- [8] R. Coisson, Phys. Rev. A 20, 524, 1979.
- [9] G. Bonvicini and J. Welch, Nucl. Inst. and Meth. 418, 223, 1998.
- [10] W. Panofsky and M. Phillips, "Classical Electromagnetism", Addison-Wesley, page 370.
- [11] J. Heintze *et al.*, Nucl. Inst. and Meth. 138, 641, 1976.
- [12] Handbook of Chemistry and Physics, 66th Edition, CRC Press, page E-198.